RSC Advances

ROYAL SOCIETY OF CHEMISTRY

www.rsc.org/advances

Fischer–Tropsch synthesis of liquid hydrocarbon over mesoporous SBA-15 supported cobalt catalysts

Yongwu Lu [a], Peng Zhou [a], Jun Han [b], and Fei Yu [a,*]

[a] Department of Agricultural and Biological Engineering, Mississippi State University, Mississippi State, MS 39762, USA

[b] Hubei Key Laboratory of Coal Conversion and New Materials, Wuhan University of Science and Technology, Wuhan 430081, China

*** Corresponding Author at:** Department of Agricultural and Biological Engineering, Mississippi State University, 130 Creelman Street, Mississippi State, MS 39762, USA Telephone: +1 662-325-3280. Fax: +1 662-325-3853. E-mail: fyu@abe.msstate.edu (F. Yu). URL: http://fy29.abe.msstate.edu (F. Yu).

Abstract: The influence of cobalt loading (10–30 wt% Co) and pore size of SBA-15 support on the physic-chemical and catalytic performance of mesoporous Co/SBA-15 catalysts for the Fischer–Tropsch synthesis (FTS) reaction (T = 245 ℃, P = 290 psig, $H_2/CO = 2$, and GHSV = 2000 h^{-1}) has been investigated. Catalysts were characterized by N_2 adsorption–desorption, X-ray diffraction (XRD), electron microscopy, and temperature-programmed reduction (TPR). The dispersion of Co/SBA-15 decreased and the extent of cobalt reduction increased with increasing either cobalt loading or pore size of SBA-15. A maximum CO conversion was found for the sample with 20wt% Co loading. More methane and less C_{5+} hydrocarbons were produced over less reducible 10 wt% Co loading sample. The 20Co/SBA-15 catalysts with larger pore led to larger cobalt

crystallite size, lower dispersion and higher reducibility. CO conversion increased with the increase of pore size in the range studied. The 20Co/SBA-15 catalysts with larger cobalt crystallite size showed higher C_{5+} selectivity for the FTS. Finally, at comparable Co loading, CO conversion of Co/SBA-15 catalysts were about 2 times than a Co/SiO_2 sample, with only minor difference in product selectivity.

Keywords: SBA-15; cobalt catalyst; Fischer–Tropsch synthesis; reducibility; dispersion

1. Introduction

Fischer–Tropsch synthesis (FTS) is a key industrial process to catalytically convert syngas (a mixture of CO and H_2) to liquid hydrocarbons via surface polymerization reaction.[1–5] In comparison to traditional petroleum-derived liquid hydrocarbons, the FTS liquid hydrocarbons are free of sulfur and aromatics pollutants,[6–8] which make them ideal candidates for the synthesis of clean transportation fuels. Syngas can be produced from various carbonaceous sources,[9–12] such as natural gas, coal, biomass, shale gas, or municipal solid waste, through steam reforming, partial or auto-thermal oxidation, or gasification processes. Therefore, the FTS process is of prominent interest to both academia and industry.

The Fischer–Tropsch (FT) reaction was shown to be catalyzed by certain transition metals including Ru, Fe, and Co.[1] Ru-based catalysts are highly active, but the Ru resource is scarce and expensive and, thus, is not commercially used.[7] Co-based FTS catalysts are usually preferred because these catalysts are more active per weight of metal, more stable toward deactivation by water (a by-product of the FTS reaction), have lower activity for the competing water-gas-shift (WGS) reaction, and produce a higher fraction of linear long-chain paraffins and less oxygenates than Fe-based catalysts.[13–18]

Supported cobalt catalysts are well-known for their activity and selectivity in the reaction of FTS.[19,20] In order to achieve a high density of surface-active sites (Co^0), cobalt precursors are usually dispersed on porous carriers, such as SiO_2, Al_2O_3, SiC, TiO_2 and so on.[13–20] Generally, the number of Co^0 active sites available for FTS depends on Co loading amount in the catalyst, the sizes of the Co particles (or dispersion), and their reducibility.[21,22] High activity of Co catalyst can be obtained as cobalt oxide is well dispersed on the support and highly reduced at desirable temperatures. FTS turnover frequencies (TOFs) were found to be independent of the cobalt dispersion and support identity over the accessible dispersion range (0.01–0.12) at typical FTS conditions.[23] Iglesia et al.[21] showed that at conditions favoring chain growth, i.e., high C_{5+} selectivity, the FTS rates per total Co atoms increase linearly with increasing metal dispersion regardless of the nature of the support used. In general, high productivity of hydrocarbons for supported cobalt-based FTS catalysts requires small cobalt crystallites at high cobalt surface densities.[24] However, the smaller the cobalt particle size, the stronger the interaction between cobalt and support, which decreases both the reducibility and activity for FTS.[24] Ideally, highly active Co-based catalysts should be prepared by achieving high dispersions of highly reducible Co species at cobalt loadings as high as possible.[13] In particular, the cobalt loading is very high at 33 g per 100 g support for the current commercial cobalt-based catalyst chosen for slurry bubble column reactor.[25] Furthermore, high cobalt loading is necessary to stabilize the catalyst against irreversible deactivation due to re-oxidation of Co^0 to cobalt oxide occurred during FTS.[26] Therefore, the support with high accessible surface area is necessary to disperse such high cobalt content.

SBA-15,[27–29] a silica-based periodic mesoporous material, is one of the most attractive catalyst supports, with high hydrothermal stability and a large surface area of 400–1000 m^2 g^{-1}, which allows for a better dispersion of a large number of catalytically active species as compared with conventional amorphous silicas.[30–33] It also has a hexagonal array of a uniform tubular channel, with a pore diameter ranging from 5 to 30 nm.[27] The ordered mesoporous silicas possessing a uniform pore size distribution should allow for a better control on the cobalt particle size, and thus, on the catalytic performance. In addition, the reducibility is favored for the SiO_2 supported Co catalyst because the strength of interaction between the cobalt and support is lower than the other commonly used support such as Al_2O_3, TiO_2 and so on.[13,34] Thus, SBA-15 is suitable for use as a potential support for the synthesis of a commercial FTS cobalt catalyst with high activity.

The increases of Co dispersion always corresponds to the decrease of reducibility for the supported cobalt due to the larger interaction surface area of Co and support.[14,35] Thus, the efficient control of cobalt dispersion and reducibility in the preparation of SBA-15-supported catalysts is of great importance to improve the FTS catalytic performance, such as activities and selectivities. Although a few studies were conducted on the effects the cobalt particle size, cobalt loading and the pore size of support on the FTS activity and selectivity, controversy persists, because these observations result from complex interplay among many factors. [3,8,20] These factors involved not only the re-adsorption probability of liquid hydrocarbon in the confined space and the diffusion situation, but also the effect of changes in the site density, such as the changes in loading, reducibility and the particle size of active metal.[3,8] Hence, it is difficult to evidence the influence of the support

porosity on activity and selectivity, since the metal dispersion or the metal particle size also depends on the pore size distribution. Therefore, more insights are expected to prepare catalysts with a fixed pore size with various metal loading, or a fixed metal loading with different pore sizes.

This work aims to address the sole effect of cobalt loading or pore size of SBA-15 on the cobalt dispersion and its reducibility, as well as on the formation of liquid hydrocarbon fuels in FTS. Both periodic SBA-15 and commercial amorphous silicas (as the control) are used as catalytic support. The catalysts are characterized by N_2 adsorption, X-ray diffraction (XRD), transmission electron microscopy (TEM), temperature-programed reduction (TPR).

2 Experimental

2.1 Catalyst preparation

The SBA-15 molecular sieves were synthesized using Pluronic triblock copolymer P123 (EO_{20}-PO_{70}-EO_{20}, M_{AV} = 5800, Aldrich) as the structure-directing agent and tetraethyl orthosilicate (TEOS) as silica source.[27] First, the triblock copolymer was dissolved in a solution of water and HCl under stirring, and then the required amount of TEOS was added to the above solution at 36 °C and kept under stirring for 20 h. Then, the gel mixture was transferred into polypropylene bottles and heated at designed aging temperature for certain time in static. The synthesis of different pores of SBA-15 depends on the aging temperature (100 or 120 °C) and aging time (24 or 48 h). After the synthesis, the solid obtained was filtered, exhaustively washed with distilled water until neutral pH,

dried at 80 °C and finally calcined in a flow of air at 500 °C for 6 h to remove the organic template.

Co catalysts supported on SBA-15 were prepared by wetness impregnation method using a solution of cobalt (II) nitrate dissolved in ethanol in excess with respect to the pore volume of the SBA-15 support (liquid/solid ratio of 4 cm^3 g^{-1}), followed by slow evaporation of the solvent in a rotary evaporator at 323 K and vacuum until dryness. The Co/SBA-15 catalysts samples were dried in an oven in 100 °C overnight then calcined in the flow of air at 450 °C for 6 h. The catalysts with different cobalt loading were labeled as *x*Co/support, and *x* referred to the weight percentage of Co loading. The 20Co/SBA-15 catalysts with different pore sizes were labeled as 20Co/SBA-15(P_i) with *i* standing for 1, 2, 3, and 4. The Co/SiO_2 catalyst was prepared by the above-mentioned wetness impregnation method.

2.2 Catalyst characterization

2.2.1 BET surface area and pore size distribution

The textural properties including, specific Brunauer-Emmett-Teller (BET) surface area, pore volume and pore diameter were measured using nitrogen absorption–desorption isotherms at –196 °C over an Autosorb-1 system (Quantachrome Instruments, Boynton Beach, FL, USA). Prior to the experiments, the samples were outgassed at 300 °C for 4 h. The BET surface areas were obtained for adsorption data in a relative pressure range from 0.05 to 0.30. The total pore volumes (TPV) were calculated from the amount of N_2 vapor adsorbed at a relative pressure close to unity (0.99), assuming that the pores are filled with the condensate in the liquid state. The pore size distribution

curves were evaluated from the desorption branches of the isotherms using the Barrett-Joyner-Halenda (BJH) formula.

2.2.2 Hydrogen temperature-programed reduction (H_2–TPR)

The reduction behavior of the supported oxidized cobalt phases was studied by TPR in a ChemBET *Pulsar* TPR/TPD equipment (Quantachrome Instruments, Boynton Beach, FL, USA). The catalyst samples were first purged in a flow of nitrogen at 300 °C for 60 min to remove traces of moisture, and then cooled to 40 °C. The TPR of 200 mg of each sample was performed using 4 % hydrogen in Argon gas mixture with a gas flow rate of 70 cm^3 min^{-1}. The samples were heated from 40 to 900 °C with a heating rate of 10 °C min^{-1}. The H_2 consumption rate was monitored in a thermal conductivity detector (TCD) calibrated previously using the reduction of CuO as standard.

2.2.3 X-ray diffraction (XRD)

The crystalline structure of SBA-15 support and Co/SBA-15 catalysts were characterized by small-angle X-ray diffraction (Rigaku SmartLab XRD, Rigaku Americas, The Woodlands, TX, USA), using Cu Kα (λ = 0.15418 nm) radiation, operated at 40 kV and 44 mA. Diffraction intensities were recorded from 0.4 to 4° at the rate of 0.12° min^{-1} with a sampling width of 0.02°. The phase composition and crystalline structure of supported cobalt catalysts were characterized by high angle X-ray diffraction (Utima III XRD, Rigaku Americas, The Woodlands, TX, USA) using Cu Kα (λ = 0.15418 nm) radiation, operated at 40 kV and 44 mA. Diffraction intensities were

recorded from 10 to 90° at the rate of 0.5° min^{-1} with a sampling width of 0.02°. The observed diffraction peaks were assigned by reference to JCPDS data.

The average crystallite sizes of Co_3O_4 in the different catalysts were estimated from the Scherrer formula of Eq. (1) [36] using the most intense reflection at 2θ = 36.9°, where $d_{(Co_3O_4)}$ is the average crystallite size of Co_3O_4, λ = 0.15418 nm is the wavelength of the target Cu Kα, θ_B is the Bragg angle. B is the line broadening by reference to a standard so that $B^2 = B_M^2 - B_S^2$, where B_M is the full width at half maximum (FWHM) of the diffracted plane of the most intense reflection at 2θ = 36.9°, and B_S is the full width at half maximum (FWHM: 0.1° 2θ) of the standard material in radians.

$$d_{(Co_3O_4)} = \frac{0.9\lambda}{B\cos\theta_B} \times \frac{180^\circ}{\pi} \quad (1)$$

The average Co_3O_4 crystallite size $d_{(Co_3O_4)}$ in the calcined samples were then converted to the corresponding mean cobalt metal diameters in reduced catalysts by considering the relative molar volumes of Co^0 and Co_3O_4 according to Eq. (2).[13]

$$d_{(Co^0)} = 0.75 \times d_{(Co_3O_4)} \quad (2)$$

Then, the Co^0 metal dispersions $D_{(Co^0)}$ can be calculated from the average Co^0 crystallite sizes $d_{(Co^0)}$ according to Eq. (3),[37,38] which assumes a spherical geometry of the metal particles with uniform site density of 14.6 atoms·nm^{-2}.

$$D_{(Co^0)} = 96/d_{(Co^0)} \quad (3)$$

2.2.4 Electron microscopy

The support and catalyst morphologies were observed using a JEOL 6500 F field emission scanning electron microscope (FE-SEM) (JEOL USA Inc., Peabody, MA, USA), operating at the accelerating voltage of 5 kV. Before the analysis, the surfaces were coated by a sputter with a thin layer (5 nm) of Pt to avoid the charging effects. Transmission electron microscope (TEM) was used to further characterize the morphology of the catalyst and to study the location of the active phase. The samples were dispersed in ethanol and sonicated for 20 min and then deposited over a Formvar copper grid to be observed in the microscope. The analyses were carried out using a JEOL 2100 electron microscope (JEOL USA Inc., Peabody, MA, USA) operating at 80 kV or 200 kV.

2.3 Catalytic tests

The Fischer-Tropsch synthesis was performed in a down-flow half-inch fixed-bed stainless steel tubular reactor. Typically, 0.5 g of catalyst diluted with quartz sand was loaded in the catalyst bed. The catalysts were reduced in situ at atmospheric pressure by passing a flow of 50%H_2/50%N_2 through the reactor. During reducing process, the temperature of reactor was increased to 400 ℃ at a heating rate of 1 ℃ min^{-1} and maintained at this temperature for 6 h. After the reduction step, the temperature was lowered to 120 ℃ under the flow of 50% H_2/50% N_2 and then the reactor pressure was slowly increased up to 290 psig by introducing the reactant syngas mixture (64% H_2 : 32% CO : balanced N_2, N_2 used as internal standard). Then, the temperature in the catalyst bed was increased from 120 to 245 ℃ at a controlled heating rate of 1 ℃ min^{-1} in order to

avoid instability of the system induced by the highly exothermic FTS reaction. Once the reaction temperature of 245 ℃ was achieved, the reaction was led to proceed during a period of 10–15 h to ensure steady state of the catalyst activity. The time on stream after achieving steady state is 120 h.

CO conversion was calculated according to Eq. (4), where F_{in} and F_{out} (mol·s^{-1}) are the total molar flow rates of the reactor inlet syngas and outlet gas, respectively, where $X_{(i),in}$ and $X_{(i),out}$ are the molar fraction of component i in the reactor inlet syngas and outlet gas.

$$\text{CO conversion (\%)} = \frac{F_{in}X_{CO,in} - F_{out}X_{CO,out}}{F_{in}X_{CO,in}} \times 100 \quad (4)$$

The product selectivity was calculated according to Eq. (5), where n_j represents the number of carbon atoms contained in product j, and X_j represents the molar fraction of product j. The C_{5+} selectivity was calculated by subtracting the amount of C_1–C_4 hydrocarbons and CO_2 in the product gas mixture from the total mass balance.

$$\text{Product selectivity (\%)} = \frac{n_j F_{out} X_j}{F_{in}X_{CO,in} - F_{out}X_{CO,out}} \times 100 \quad (5)$$

The consumption rate of CO, r_{CO} ($mol \cdot s^{-1} \cdot mol_{Co^0}{}^{-1}$) was calculated according to Eq. (6), where n_{Co^0} (mol) is the mole of Co^0 of the reduced catalyst in this reaction.

$$-r_{CO} = \frac{F_{in}X_{CO,in} - F_{out}X_{CO,out}}{n_{Co^0}} \quad (6)$$

The formation rate of CO_2, r_{CO_2} ($mol \cdot s^{-1} \cdot mol_{Co^0}{}^{-1}$) was calculated according to Eq. (7), where $X_{CO_2,out}$ is the mole fraction of CO_2 in the reactor outlet gas, and n_{Co^0} (mol) is the mole of Co^0 of the reduced catalyst in this reaction.

$$r_{CO_2} = \frac{F_{out}X_{CO_2,out}}{n_{Co^0}} \quad (7)$$

The reaction rate of Fischer–Tropsch synthesis (FTS), r_{FTS} ($mol \cdot s^{-1} \cdot mol_{Co^0}{}^{-1}$) was calculated according to Eq. (8).

$$r_{FTS} = -r_{CO} - r_{CO_2} = \frac{F_{in}X_{CO,in} - F_{out}X_{CO,out} - F_{out}X_{CO_2,out}}{n_{Co^0}} \quad (8)$$

2.4 Product analysis

The outlet gaseous products were composed of C_1–C_4 ranged hydrocarbons, H_2, CO, CO_2, and N_2 were analyzed by using an online Agilent 7890 GC instrument, equipped with one flame ionization detector (FID) and two thermal conductivity detectors (TCDs). C_1–C_4 ranged hydrocarbons were analyzed by using a HP-Plot Al_2O_3 capillary column (50 m × 530 μm ID) with a FID and N_2 carrier. CO, CO_2, and N_2 were analyzed by using molecular sieve-packed column with a TCD and He carrier. H_2 was analyzed by using molecular sieve-packed column with a TCD and N_2 carrier.

During the reaction the reactor outlet gas passed sequentially through a hot trap (T = 120 °C, P = 290 psig) to collect waxes and water, and a cold trap (T = –5 °C) to collect residual liquid oil and water. A small fraction of the wax product collected from hot trap at 120 °C was first dissolved in CS_2 (0.7 wt% of wax) and then analyzed off-line using a gas chromatograph coupled to a mass spectrometer (GC–MS) equipped with an Agilent 6890 series gas chromatograph system, an Agilent 7863B series injector, a 5973 mass selective detector, and a flame ionization detector (FID). An OV-101 capillary column (FID, N_2 carrier) was used with the temperature programmed (2 ℃ min^{-1}) from 50 to 300 ℃.

The liquid oil product collected from cold trap at –5 °C were analyzed off-line using a gas chromatograph coupled to a mass spectrometer (GC–MS) equipped with an Agilent

6890 series gas chromatograph system, an Agilent 7863B series injector, a 5973 mass selective detector, and a flame ionization detector (FID). An Agilent HP-5 capillary column was used for analyzing hydrocarbons, and an Agilent DB-WAXetr (50 m × 0.32 mm I.D., 1.0 μm) capillary column was used for analyzing aqueous phase product that including oxygenated compounds and water, while water was quantified according to an external standard method. Helium was the carrier gas with a flow rate of 1 mL min^{-1}. The temperatures of the injector and detector were both kept at 250 ℃. The oven was maintained at 40 ℃ for 5 min, ramped to 250 ℃ by 10 ℃ min^{-1}, and then held at this temperature for 10 min. For the mass spectrometer (MS), temperatures of the transfer line and electron impact (EI) source were 250 and 200 ℃, respectively.

The hydrocarbon chain length distribution is given by the Anderson–Schulz–Flory (ASF) distribution.[8] The chain growth probability, α, can be calculated according to Eq. (9):[8]

$$\ln\left(\frac{W_n}{n}\right) = n\ln\alpha + const. \quad (9)$$

where W_n is the mass fraction of the species with carbon number n. From the slope of the plot of $\ln\left(\frac{W_n}{n}\right)$ against n, the value of α can be obtained.

3. Results and discussion

3.1 Support and catalyst characterization

3.1.1 Nitrogen adsorption/desorption

Upon N_2 adsorption, SBA-15 and Co/SBA-15 produce irreversible type IV isotherms with a H1 hysteresis loop (Fig. 1a) that is typical of mesoporous materials with

1D cylindrical channels.[35] The N_2 adsorption–desorption isotherm for calcined siliceous SBA-15 exhibited a sharp inflection at a relative pressure in the range of 0.7–0.8 (Fig. 1a), which demonstrated a good quality of SBA-15 material with uniform mesopores.[39,40] The shape of the N_2 adsorption–desorption isotherms of Co-supported SBA-15 catalysts containing ca. 10, 20, and 30wt% Co as shown in Fig. 1a, was similar to that of the SBA-15 support, which indicated that the mesoporous structure of SBA-15 was largely maintained upon cobalt impregnation.[13]

The inflection of the adsorption branch of the isotherm occurred at a lower relative pressure (0.65–0.75) for Co-containing samples as compared to the pure mesoporous silica SBA-15, suggesting a decrease of the average pore diameter after cobalt impregnation.[13] The average pore diameter of the pure silica SBA-15 obtained from N_2 adsorption at –196 °C using the BJH method was 8.0 nm, while it decreased to about 7.1 nm for the 30wt% Co/SBA-15 catalyst sample (see Table 1). The N_2 adsorption–desorption isotherm for 20Co/SiO_2 catalyst is shown in Fig. 1b. The N_2 adsorption–desorption isotherms and the corresponding pore size distributions calculated from N_2 desorption isotherms for 20Co/SBA-15 catalysts with different pore sizes (4.9, 6.5, 7.8, and 9.7 nm) are presented in Fig. 1c and 1d, respectively.

The chemical composition and textural properties obtained by N_2 adsorption–desorption of the pure silica SBA-15 sample and supported cobalt catalysts samples are given in Table 1. The BET surface area and total pore volume of the siliceous calcined SBA-15 are 460 $m^2\ g^{-1}$ and 1.85 $cm^3\ g^{-1}$, respectively, which are typical for SBA-15 synthesized under similar conditions.[13,27,28] Both the BET surface area and the total pore volume significantly decreased upon Co being impregnated, with greater decrease at

higher Co loading (Table 1). This may result from a partial blockage of the SBA-15 pores by cobalt oxide clusters and/or a partial collapse of the mesoporous structure.[13] As shown in Table 1, SBA-15 gives the BET surface area of 460 m^2 g^{-1}, which is much larger than that of commercial silica SiO_2 (154 m^2 g^{-1}). The pore size of SBA-15 (8.0 nm) is much smaller than that of SiO_2 (23.3 nm).

3.1.2 Electron microscopy

Scanning electron microscopy (SEM) images (Fig. 2) revealed that the as-synthesized SBA-15 sample consists of many rope-like domains (Fig. 2b, low magnification) with relatively uniform sizes of ~1 μm, which aggregated into wheat-like macrostructures (Fig. 2a, high magnification), which agreed with the observation reported by Zhao et al.[27,28] Wheat-like mesoporous SBA-15 can have a long aspect of as much as several hundred micrometers, with a relatively uniform diameter of ~10 μm that is made up of a bundle of wires (diameter ~300 nm). TEM images showed the highly ordered hexagonal arrangement of the channels along two directions, parallel (Fig. 3c) and perpendicular (Fig. 3d).

HRTEM images of calcined 20Co/SBA-15 catalysts with different pore sizes (4.9, 6.5, 7.8, and 9.7 nm) are shown in Fig. 3. The highly ordered hexagonal arrangement of the channels along the direction parallel to the *c* axis. The mesoporous structure of SBA-15 was clearly retained after cobalt impregnation and calcination. The average particle sizes of 20Co/SBA-15 with different pore sizes are 13.8, 8.9, 19.1 and 16.1 nm, respectively. The insets shown in Fig. 3 are the corresponding cobalt particle size distributions. The observed TEM cobalt particles were larger than pore size of SBA-15

support, because the cobalt particles were distributed both inside (small grey particle < pore size) and outside (relative big dark particle > pore size) the pore channels of SBA-15. The discrepancies found between the Co_3O_4 crystallite sizes obtained from XRD (Table 1) and Co_3O_4 particle sizes observed from TEM may be due to the partial agglomeration of cobalt particles during TEM sample preparation.

3.1.3 X-ray diffraction (XRD)

XRD patterns of 20Co/SBA-15 and 20Co/SiO_2 are presented in Fig. 4a. Co_3O_4 is the only detectable crystalline cobalt species present after catalyst calcination. Diffraction peaks at 2θ of 19.0. 31.3, 36.9, 44.8, 59.4 and 65.2 indicate that after calcination, cobalt was present in the form of crystalline Co_3O_4 spinel on all of the catalysts,[13] which agreed with JCPDS no. 42-1467. The only difference between the XRD patterns of the calcined samples was the width of the Co_3O_4 peaks. For all catalysts, the Co_3O_4 crystallite size (Table 1) was calculated from the (311) diffraction at $2\theta = 36.9°$ according to the Scherrer equation.[36] The average Co_3O_4 crystallite size was calculated to be 27.1 nm for 20Co/SiO_2, while it was calculated to be 14.9 nm for 20Co/SBA-15. The smaller crystallite size indicated better cobalt dispersion for 20Co/SBA-15 than 20Co/SiO_2.[41–44] HRTEM image (Fig. 4b) further confirms that cobalt was present in the form of Co_3O_4 crystalline phase after calcination. The interplanar spacing *d* was measured to be 0.287 and 0.208 nm, which was characteristic of Co_3O_4 (220) and (400), respectively.

The small-angle XRD pattern (Fig. 5a) for as synthesized (after calcination in air at 500 ℃ for 6 h) mesoporous silica (SBA-15) mainly showed one peak at $2\theta = 0.7°$ that was indexable as (100) reflection associated with *p6mm* hexagonal symmetry.[27,28] After

loading with cobalt catalyst (Fig. 5a), the mesoporous structures of SBA-15 were well preserved, confirming the hexagonal SBA-15 is thermally stable.

The high-angle XRD patterns for the Co/SBA-15 catalysts with different cobalt loading (10–30 wt%) are shown in Fig. 5b. Diffraction peaks at 2θ of 19.0. 31.3, 36.9, 44.8, 59.4 and 65.2 indicated that after calcination, cobalt was present in the form of crystalline Co_3O_4 spinel on all of the catalysts,[13] which agreed with JCPDS no. 42-1467. The small-angle and high-angle XRD patterns of Co/SBA-15 catalysts with different pore sizes of SBA-15 support are presented in Fig. 5c and 5d. The only difference between the XRD patterns of the calcined samples was the width of the Co_3O_4 peaks. For all catalysts, the Co_3O_4 crystallite size (Table 1) was calculated from the most intense reflection peak (311) at $2\theta = 36.9°$ according to the Scherrer equation.[36]

3.1.4 Hydrogen temperature programmed reduction (H_2–TPR)

The H_2–TPR profiles have been normalized per weight of cobalt in the catalyst to facilitate the discussion. The influence of Co loading on the reduction behavior for Co/SBA-15 catalysts calcined at 450 ℃ is shown in Fig. 6a. One main reduction peak that can be deconvoluted to two peaks close to each other with temperature maxima at about 333–374 ℃ ($T1_{max}$) and 356–398 ℃ ($T2_{max}$), respectively, was observed. The first peak could be assigned to reduction of Co_3O_4 to CoO, and the second one to be the subsequent reduction of CoO to Co^0.[13,14,45,46] The calculated $T2_{max}/T1_{max}$ deconvoluted peak area ratio were 0.47, 0.26, and 0.20 for 10, 20, and 30Co/SBA-15 catalysts, respectively. The $T2_{max}/T1_{max}$ deconvoluted peak area ratio decreased with Co loading, indicating a higher reduction degree of CoO to metallic Co with increasing the average

diameter of Co_3O_4 particles. Besides these main reduction peaks, two broad reduction features in the temperature range of 410–600 ℃ and 600–850 ℃ were also observed, suggesting the presence of surface Co-support species with different degrees of interactions between them.[13,23]

As shown in Fig. 6a, the relative ratio of the species reducing at high temperature (600–800 ℃) to the overall reduction pattern decreased and the maximum temperature for these species shifted to lower temperature, which indicates a lower strength of interaction between cobalt and SBA-15 support, with increasing Co loading. Such a high reduction temperature may be ascribed to the reduction of cobalt silicate species formed during the TPR experiments by the reaction of highly dispersed CoO with the siliceous SBA-15.[13] Actually, cobalt silicate species were reported to be reduced at temperatures above 450 ℃,[47] while bulk Co_3O_4 became completely reduced at temperatures below 500 ℃.[48,49] Therefore, most of the cobalt in the calcined 10Co/SBA-15 sample strongly interacted with the SBA-15 support, and 30Co/SBA-15 sample had a weaker interaction between cobalt and SBA-15 support.

The TPR spectra of 20wt% Co/SBA-15 catalyst with different pore sizes are shown in Fig. 6b. One main reduction peak that can be deconvoluted to two peaks close to each other with temperature maxima at about 349–371 ℃ ($T1_{max}$) and 367–388 ℃ ($T2_{max}$), respectively, was observed. This peak resulted from the reduction of Co_3O_4 to CoO, and subsequently to Co^0.[13,14,45,46] The different cobalt loading, the varied Co_3O_4 crystallite size and dispersion. Thus, the reduction peak temperature varied with different loading. The calculated $T2_{max}/T1_{max}$ deconvoluted peak area ratio were 0.40, 0.50, 0.16 and 0.30 for 20Co/SBA-15 catalysts with pore sizes of 4.9, 6.5, 7.8, and 9.7 nm, respectively. Two

broad reduction features in the temperature of 450–600 ℃ and 600–850 ℃ were also observed, suggesting the presence of surface Co-support species with different degrees of interaction between them. As the pore size of SBA-15 increases, the broad peaks (600–850 ℃) shifted to lower temperature, and the relative contribution of species reducing at the high temperature to the overall reduction pattern decreased, which indicated a lower strength of interaction between cobalt and SBA-15 support. All these indicated that the smaller pore size of Co/SBA-15 catalysts were more difficultly reduced.

Alternatively, two reduction peaks of SiO_2 supported cobalt catalyst were observed (Fig. 6c), which can be deconvoluted to five peaks. The first peak located at 383 ℃ corresponds to the reduction of Co_3O_4 to CoO, and the second peak at 406 ℃ indicates the reduction of CoO to Co.[13,45,46] The temperature of two stage reduction of Co_3O_4 of 20Co/ SiO_2 was more higher (~ 10 ℃) than that of 20Co/SBA-15. In addition, the third, fourth, and fifth peaks at 498, 550, and 576 ℃, respectively, were observed, which indicates more difficult reduction process possibly due to stronger cobalt oxide-SiO_2 support interaction.

3.1.5 Relationship of cobalt reducibility with cobalt crystallite size, cobalt dispersion and SBA-15 pore size

The extent of Co reduction estimated from the amount of H_2 consumed of TPR profiles below 400 ℃ is given in Table 1. Fig. 7 shows that the cobalt reducibility increases with increasing the sizes of Co_3O_4 crystallites, and the cobalt reducibility decreases with increasing the cobalt dispersion on SBA-15 support. The extent of reduction of Co/SBA-15 samples prepared from cobalt nitrate increased from 48 to 86%

when increasing the Co loading from 10 to 30wt% (Table 1). In a previous characterization study, Khodakov et al.[35] found that the hydrogen reduction properties of supported cobalt oxide particles depended on the size of the Co_3O_4 crystallites, with larger particles being easily reduced. This finding is in agreement with our observed increase of reducibility with increasing Co_3O_4 crystallite size in the *x*Co/SBA-15 series with different Co loadings.

Characterization results (Table 1) showed that the catalyst porosity played an important role in the structure and reducibility of supported cobalt species. The size of supported Co_3O_4 crystallites measured by XRD was found to depend on pore sizes, as smaller Co_3O_4 particles being observed in narrow pore SBA-15 (Table 1). The dependence of Co_3O_4 crystallite sizes on catalyst pore diameters suggested preferential localization of Co_3O_4 particle in silica pores (Table 1). It was shown that narrow pore size distribution in periodic mesoporous silicas could stabilize supported nanoparticles.[50,51] Zhang et al.[50] reported the procedure to prepare nanosized ZnS particles in ordered mesoporous silicas. Iwamoto et al.[51] showed that MCM-41 materials could stabilize nanoparticles of iron oxides. Therefore, the sizes of Co_3O_4 particles in mesoporous silica could be controlled by pore sizes of SBA-15.

Fig. 8 shows that the sizes of Co_3O_4 crystallites and the cobalt reducibility depended on the average pore diameters in SBA-15; larger Co_3O_4 crystallites were found in SBA-15 with wider pores. Differences in Co_3O_4 crystallites sizes result in difference in cobalt reducibility. As shown in Fig. 8, small cobalt particles in narrow pores were more difficult to reduce than larger particles in wide pores. It is known that reducibility of Co_3O_4 crystallites depends on their sizes; the ease of reduction increasing from smaller to

larger particles.[35] It was suggested that the interaction between metal and support in smaller particles was much stronger than in larger particles and this interaction was likely to stabilize small oxidized particles and clusters in silica.[52 –54] The reducibility of Co species is higher in larger pore of SBA-15, because larger pore SBA-15 contain larger, and thus easier to reduce, Co_3O_4 crystallites.[13,35] Therefore, SBA-15 porosity influences the structure of Co supported species in two ways: first, the size of encapsulated Co species is controlled by the pore diameter of the SBA-15 support; second, cobalt reducibility is affected by SBA-15 porosity, and the reducibility of cobalt species being much larger in wide pore SBA-15 supports.

3.2 Fischer–Tropsch synthesis

3.2.1 Activity of Co/SBA-15 catalysts

3.2.1.1 Effect of cobalt loading

The catalytic activity of the different Co/SBA-15 catalysts was studied in a fixed-bed reactor under FTS reaction conditions: P = 290 psig, T = 245 ℃, H_2/CO = 2, GHSV = 2000 h^{-1}. The activity and selectivity values reported here corresponded to the period of steady-state behavior. The catalytic results are summarized in Table 2. CO conversion had a maximum at a cobalt loading of 20wt%. CO conversion increased from 18.3% (10Co/SBA-15) to 35.6% (20Co/SBA-15), then decreased to 22.4% (30Co/SBA-15). In general, the activity of reduced Co catalysts should be proportional to the concentration of surface Co^0 sites.[21] As observed in Fig.9, the steady-state FTS reaction rate calculated on the basis of reduced cobalt with different cobalt loading increased as a function of Co^0 dispersion. The maximum activity obtained thus reflected the inverse trend of cobalt

dispersion and direct trend of extent of reduction observed when increasing Co loading. However, the maximum concentration of surface Co^0 sites was achieved for the 20wt% Co sample exhibiting a balanced of good dispersion and high reducibility. It can also be seen from Table 2 that at similar cobalt loading (20wt%), CO conversion based on the mesoporous SBA-15 support is about 2 times than that based on amorphous silica. This higher activity can be attributed to a higher dispersion of cobalt on the high surface area mesoporous support (Table 1) and a larger reducibility of cobalt oxide (Table 1 and Fig. 6c).

3.2.1.2 Effect of pore size of SBA-15 support

Catalytic data show that CO conversion were much lower on Co catalysts with 20wt% loading supported by narrow pore materials. As shown in Table 2, CO conversion increased from 27.6% to 43.8% as the pore size of SBA-15 increased from 4.9 nm [20Co/SBA-15(P1)] to 9.7 nm [20Co/SBA-15(P4)] in the range studied. As observed in Fig. 10, the steady-state FTS reaction rate calculated based on reduced cobalt with different pore size of SBA-15 support increased as a function of Co^0 dispersion. Catalyst characterization revealed that narrow pore catalysts contained smaller cobalt crystallites (Table 1). Thus, the activity of the catalysts seems to be affected by the size of cobalt crystallites. Xiong et al.[24] found that CO conversion of Co/SBA-15 catalysts with high cobalt loading (30wt%) prepared by impregnation method increased from 19.3% to 30.9% as SBA-15 pore size increased from 3.7 to 9.0 nm. They showed that the catalyst with larger pore led to larger cobalt cluster size, lower dispersion and higher reducibility. The larger pores created more adsorbed CO of the bridge-type on FTS based on Diffuse

Reflectance Infrared Fourier Transform Spectroscopy (DRIFS) study. It was also suggested that FTS was structure sensitive and favored sites to which CO was strongly coordinated. It was suggested that partially reduced cobalt species did not catalyze FTS and that small particles could be easily re-oxidized by water or other reaction products at the conditions of FTS.[35] Our data are consistent with the suggestion that lower activity of small cobalt crystallites could be attributed to their lower reducibility.

3.2.2 Product selectivity of Co/SBA-15 catalysts

3.2.2.1 Effect of cobalt loading

The selectivity to different FTS products obtained for different cobalt loadings is presented in Table 2. It can be seen that the Co/SBA-15 with 10–30wt% Co loading exhibited a high selectivity toward hydrocarbons (90.4–93.3%), and low selectivity toward alcohols (5.6–7.8%) and CO_2 (1.1–1.8 %) reflecting a low activity for the competitive water-gas-shift reaction (WGS: $CO + H_2O \rightarrow CO_2 + H_2$) typically observed for Co-based FTS catalysts.[13] A higher concentration of light product (CH_4, C_2–C_4) among the hydrocarbon fraction was observed for the low cobalt loaded catalyst. High methane selectivity has also been reported for low cobalt loaded catalysts with small particle, high dispersion and low reducibility.[37] This effect was ascribed to diffusion limitations for CO in catalyst pores could increase H_2/CO ratio in catalyst pore and thus, methane selectivity.[55] The chain growth probability, α, derived from the slopes of the Anderson–Shultz–Flory (ASF) plots in the C_8–C_{14} hydrocarbon range did not change with different Co loadings (Table 2). The formation of C_{5+} hydrocarbons was favored over Co/SBA-15 catalysts exhibiting low cobalt dispersion and high reducibility. As

shown in Fig. 11, as the cobalt loading increased from 10 to 30wt%, the selectivity to C_{5+} hydrocarbons increased from 61.4 to 63.9 %.

3.2.2.2 Effect of pore size of SBA-15 support

The selectivity to different FTS products obtained for different SBA-15 pore sizes is also presented in Table 2. The decrease in pore sizes resulted in higher methane selectivity, whereas the chain growth probability, α, seemed not to be affected by variation in catalyst pore diameters. Analysis of literature data shows that higher methane selectivities are observed in FTS when Co catalysts are not completely reduced or contain smaller cobalt particles.[24] Thus, higher methane selectivities observed on narrow pore SBA-15 are likely to be attributed to the presence of either unreduced cobalt species or the small cobalt particles, which produce higher relative amounts of methane than large cobalt particles. Table 2 also show that lower C_{5+} selectivity observed on narrow pore samples is likely to be related not only to lower probability of chain propagation of narrow pore silicas, but also to higher methane selectivity. As shown in Fig. 12, as the pore size of SBA-15 increased from 4.9 to 9.7 nm, the selectivity to C_{5+} hydrocarbons increased from 62.2 to 64.6 %. This was attributed to the increase of pore size of SBA-15, which decreased the cobalt dispersion, and thus increased the cobalt reducibility.

4. Conclusions

A series of SBA-15 supported cobalt catalysts with different cobalt loading and different pore diameters have been prepared and the role of cobalt loading and pore size on FTS have been investigated. The reduction of the catalysts took place in two stages,

with Co_3O_4 reduction to CoO and subsequently to Co^0. The dispersion of Co/SBA-15 decreased and the extent of cobalt reduction increased with increasing either cobalt loading or pore size of SBA-15. A maximum CO conversion was found for the sample with 20wt% Co loading. More methane and less C_{5+} hydrocarbons were produced over less reducible 10wt% Co loading sample. The 20Co/SBA-15 catalysts with larger pore led to larger cobalt crystallite size, lower dispersion, and higher reducibility. CO conversion increased with the increase of pore size in the range studied. The 20Co/SBA-15 catalysts with larger cobalt crystallite size showed higher C_{5+} selectivity for the FTS. Finally, at comparable Co loading, CO conversion of Co/SBA-15 catalysts were about 2 times than a Co/SiO_2 sample, with only minor difference in product selectivity.

Acknowledgements

Financial support provided by the Cooperative State Research, Education, and Extension Service, and U.S. Department of Agriculture, under the Award No. 2012–10008–20302.

References

1 A. Y. Khodakov, W. Chu and Fongarland P, *Chem. Rev.*, 2007, **107**, 1692.

2 Y. Zhang, L. Ma, T. Wang and X. Li, *RSC Adv.*, 2015, **5**, 45426.

3 Y. Liu, J. -F. Chen and Y. Zhang, *RSC Adv.*, 2015, **5**, 29002.

4 O. O. James, B. Chowdhury, M. A. Mesubi and S. Maity, *RSC Adv.*, 2012, **2**, 7347.

5 J. C. Park, D. H. Chun, J. -i. Yang, H. -T. Lee, S. Hong, G. B. Rhim, S. Jang and H. Jung, *RSC Adv.*, 2015, **5**, 44211.

6 Q. Yan, Y. Lu, C. Wan, J. Han, J. Rodriguez, J. Yin and F. Yu, *Energy Fuels*, 2014, **28**, 2027.

7 E. de Smit and B. M. Wechhuysen, *Chem. Soc. Rev.*, 2008, **37**, 2758.

8 Q. Zhang, J. Kang and Y. Wang, *ChemCatChem*, 2010, **2**, 1030.

9 Y. Lu, B. Cao, F. Yu, J. Liu, Z. Bao and J. Gao, *ChemCatChem*, 2014, **6**, 473.

10 J. Hu, F. Yu and Y. Lu, *Catalysts*, 2012, **2**, 303.

11 S. Luo, L. Zeng, D. Xu, M. Kathe, E. Chung, N. Deshpande, L. Qin, A. Majumder, T. Hsieh, A. Tong, Z. Sun and L. Fan, *Energy Environ. Sci.*, 2014, **7**, 4104.

12 J. Wang, G. Cheng, Y. You, B. Xiao, S. Liu, P. He, D. Guo, X. Guo and G. Zhang, *Int. J. Hydrogen Energy*, 2012, **37**, 6503.

13 A. Martínez, C. López, F. Márquez and I. Díaz, *J. Catal.*, 2003, **220**, 486.

14 L. Yu, X. Liu, Y. Fang, C. Wang and Y. Sun, *Fuel*, 2013, **112**, 483.

15 A. R. de la Osa, A. de Lucas, L. Sánchez-Silva, J. Díaz-Maroto, J. L. Valverde and P. Sánchez. *Fuel*, 2012, **95**, 587.

16 S. Sun, K. Fujimoto, Y. Yoneyama and N. Tsubaki, *Fuel*, 2002, **81**, 1583.

17 W. Ma, G. Jacobs, D. E. Sparks, M. K. Gnanamani, V. R. R. Pendyala, C. H. Yen, J. L. S. Klettlinger, T. M. Tomsik and B. H. Davis, *Fuel*, 2011, **90**, 756.

18 P. R. Karandikar, Y. J. Lee, G. Kwak, M. H. Woo, S. J. Park, H. G. Park, K. S .Ha and K. W. Jun, *J. Phys. Chem. C*, 2014, **118**, 21975.

19 J. Zhang, J. Chen, J. Ren, Y. Li and Y. Sun, *Fuel*, 2003, **82**, 581.

20 J. S. Girardon, E. Quinet, A. Griboval-Constant, P. A. Chernavskii, L. Gengembre and A. Y. Khodakov, *J. Catal.*, 2007, **248**, 143.

21 E. Iglesia, S. L. Soled and R. A. Fiato, *J. Catal.*, 1992, **137**, 212.

22 B. G. Johnson, C. H. Bartholomew and D. W. Goodman, *J. Catal.*, 1991, **128**, 231.

23 E. Iglesia, *Appl. Catal. A*, 1997, **161**, 59.

24 H. Xiong, Y. Zhang, K. Liew and J. Li, *J. Mol. Catal. A Chem.*, 2008, **295**, 68.

25 G. Jacobs, Y. Y. Ji, B. H. Davis, D. Cronauer, A. J. Kropf and C. L. Marshall, *Appl. Catal.A*, 2007, **333**, 177.

26 P. J. van Berge, J. van de Loosdrecht, S. Barradas and A. M. van der kraan, *Catal. Today*, 2000, **58**, 321.

27 D. Zhao, J. Feng, Q. Huo, N. Melosh, G. H. Fredrickson, B. F. Chmelka and G. D. Stucky, *Science*, 1998, **279**, 548.

28 D. Zhao, J. Sun, Q. Li and G. D. Stucky, *Chem. Mater.*, 2000, **12**, 275.

29 M. Shakeri, R. J. M. Klein Gebbink, P. E. de Jongh and K. P. de Jong, *Angew. Chem. Int. Ed.*, 2013, **52**, 10854.

30 G. Prieto, A. Martínez, R. Murciano and M. A. Arribas, *Appl. Catal. A*, 2009, **367**, 146.

31 H. Li, J. Li, H. Ni and D. Song. *Catal. Lett.*, 2006, **110**, 71.

32 O. González, H. Pérez, P. Navarro, L. C. Almeida, J. G. Pacheco and M. Montes, *Catal. Today*, 2009, **148**, 140.

33 A. Y. Khodakov, R. Bechara and A. Griboval-Constant, *Appl. Catal. A*, 2003, **254**, 273.

34 Y. Wang, M. Noguchi, Y. Takahashi and Y. Ohtsuka, *Catal. Today*, 2001, **68**, 3.

35 A. Khodakov, A. Griboval-Constant, R. Bechara and V. L. Zholobenko, *J. Catal.*, 2002, **206**, 230.

36 Y. Lu, F. Yu, J. Hu and J. Liu, *Appl. Catal. A*, 2012, **429–430**, 48.

37 R. C. Reuel and C. H. Bartholomew, *J. Catal.*, 1984, **85**, 63.

38 R. D. Jones and C. H. Bartholomew, *Appl. Catal.*, 1988, **39**, 77.

39 Z. Luan, M. Hartmann, D. Zhao, W. Zhou and L. Kevan, *Chem. Mater.*, 1999, **11**, 1621.

40 Z. Luan, E. M. Maes, P. A. W. van der Heide, D. Zhao, R. S. Czernuszewicz and L. Kevan, *Chem. Mater.*, 1999, **11**, 3680.

41 G. L. Bezemer, J. H. Bitter, H. P. C. E. Kuipers, H. Oosterbeek, J. E. Holewijn, X. Xu, F. Kapteijn, A. Jos van Dillen and K. P. de Jong, *J. Am. Chem. Soc.*, 2006, **128**, 3956.

42 J. P. den Breejen, P. B. Radstake, G. L. Bezemer, J. H. Bitter, V. Frøseth, A. Holmen and K. P. de Jong, *J. Am. Chem. Soc.*, 2009, **131**, 7197.

43 G. Prieto, A. Martínez, P. Concepción and R. Moreno-Tost, *J. Catal.*, 2009, **266**, 129.

44 Ø. Borg, P. D. C. Dietzel, A. I. Spjelkavik, E. Z. Tveten, J. C .Walmsley, S. Diplas, S. Eri, A. Holmen and E. Rytter, *J. Catal.*, 2008, **259**, 161.

45 P. Arnoldy and J. A. Moulijn, *J. Catal.*, 1985, **93**, 38.

46 B. Viswanathan and R. Gopalakrishnan, *J. Catal.*, 1986, **99**, 342.

47 B. Sexton, A. Hughes and T. Turney, *J. Catal.*, 1986, **97**, 390.

48 S. Bessell, *Appl. Catal. A*, 1993, **96**, 253.

49 G. Sewell, C. O'Connor and E. van Steen, *Appl. Catal. A*, 1995, **125**, 99.

50 W. H. Zhang, J. L. Shi, H. R. Chen, Z. L. Hua and D. S. Yan, *Chem. Mater.*, 2001, **13**, 648.

51 M. Iwamoto, T. Abe and Y. Tachibana, *J. Mol. Catal. A Chem.*, 2000, **155**, 143.

52 A. Y. Khodakov, A. Griboval-Constant, R. Bechara and F. Villain, *J. Phys. Chem. B*, 2001, **105**, 9805.

53 R. Bechara, D. Balloy, J. Y. Dauphin and J. Grimblot, *Chem. Mater.*, 1999, **11**, 1703.

54 A. Y. Khodakov, J. Lynch, D. Bazin, B. Rebours, N. Zanier, B. Moisson and P. Chaumette, *J. Catal.*, 1997, **168**, 16.

55 R. B. Anderson, W. K. Hall, A. Krieg and B. Seligman, *J. Am. Chem. Soc.*, 1949, **71**, 183.

Figures and Tables

Fig. 1 Nitrogen adsorption–desorption isotherms obtained at –196 °C for (a) SBA-15, 10Co/SBA-15, 20Co/SBA-15, and 30Co/SBA-15, (b) 20Co/SiO_2 and 20Co/SBA-15, (c) 20Co/SBA-15(P1), 20Co/SBA-15(P2), 20Co/SBA-15(P3), and 20Co/SBA-15(P4), and (d) the corresponding pore size distribution curves calculated from N_2 desorption–desorption isotherms of (c).

Fig. 2 SEM images of as-synthesized hexagonal mesoporous silica SBA-15 at (a) low magnification and (b) high magnification, and TEM images of SBA-15 by the direction of (c) parallel and (d) perpendicular.

Fig. 3 HRTEM images of calcined 20Co/SBA-15 catalysts (a) 20Co/SBA-15(P1), (b) 20Co/SBA-15(P2), (c) 20Co/SBA-15(P3), and (d) 20Co/SBA-15(P1). The insets are the cobalt particle size distributions.

Fig. 4 (a) XRD patterns of calcined 20Co/SiO_2 and 20Co/SBA-15 catalysts, and (b) HRTEM images of 20Co/SBA-15 catalyst.

Fig. 5 (a) Small-angle XRD patterns of SBA-15 and Co/SBA-15 catalysts with different cobalt loadings, (b) high-angle XRD patterns of Co/SBA-15 with different cobalt loadings, (c) small-angle and (d) high-angle XRD patterns of Co/SBA-15 catalysts with different pore sizes of SBA-15 support.

Fig. 6 Temperature programmed reduction profiles of calcined cobalt catalysts.

Fig. 7 Relationship between Co_3O_4 crystallite size, cobalt dispersion and its reducibility.

Fig. 8 Dependences of Co_3O_4 crystallite sizes and extents of Co reduction at 400 ℃ on the different pore diameters of SBA-15.

Fig.9 FTS reaction rate based on reduced cobalt with different cobalt loading as a function of Co^0 dispersion.

Fig.10 FTS reaction rate based on reduced cobalt with different pore size of SBA-15 support as a function of Co^0 dispersion.

Fig. 11 Effect of cobalt loading on cobalt dispersion and C_{5+} selectivity.

Fig. 12 Effect of pore diameter of SBA-15 on cobalt dispersion and C_{5+} selectivity.

Table 1 Properties of the supports and catalysts determined by N_2 adsorption, XRD and TPR characterization.

Table 2 FTS results for Co/SBA-15 catalysts.

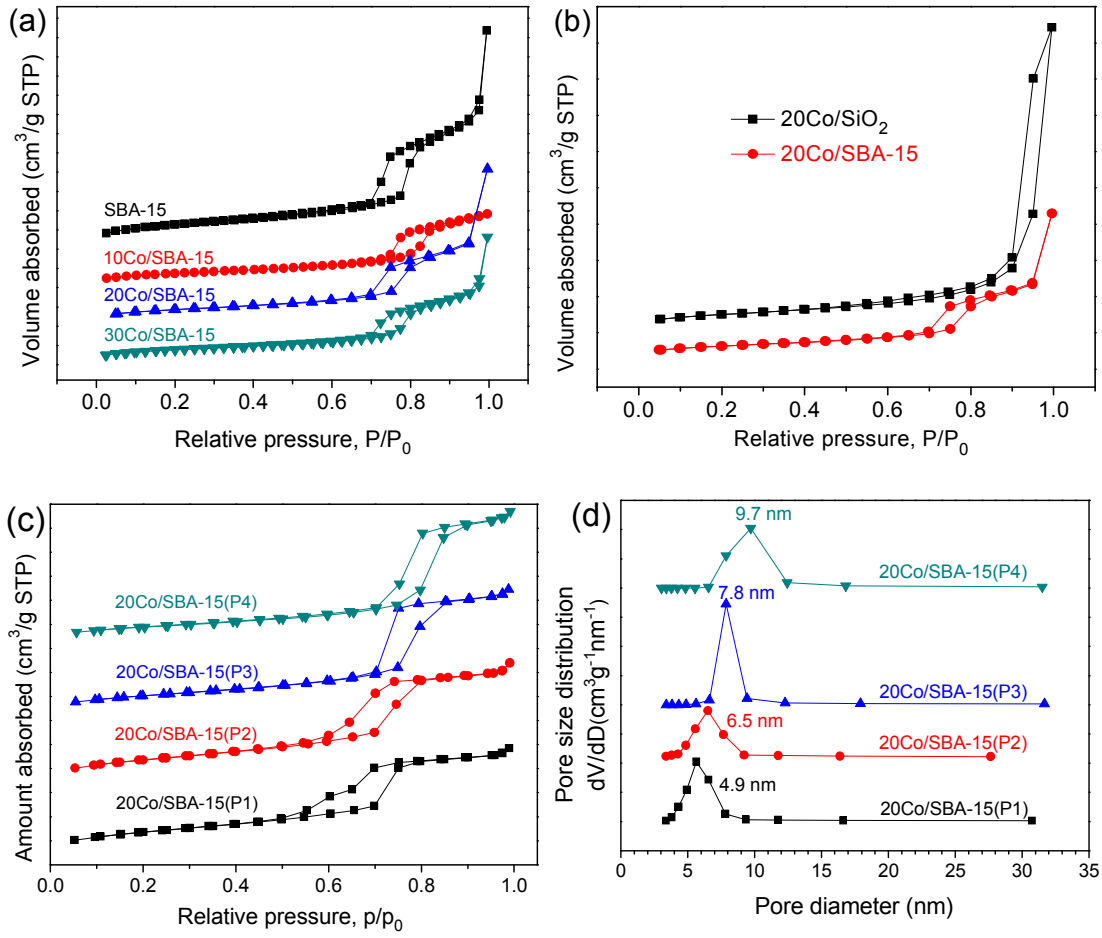

Fig. 1 Nitrogen adsorption–desorption isotherms obtained at –196 °C for (a) SBA-15, 10Co/SBA-15, 20Co/SBA-15, and 30Co/SBA-15, (b) 20Co/SiO_2 and 20Co/SBA-15, (c) 20Co/SBA-15(P1), 20Co/SBA-15(P2), 20Co/SBA-15(P3), and 20Co/SBA-15(P4), and (d) the corresponding pore size distribution curves calculated from N_2 desorption–desorption isotherms of (c).

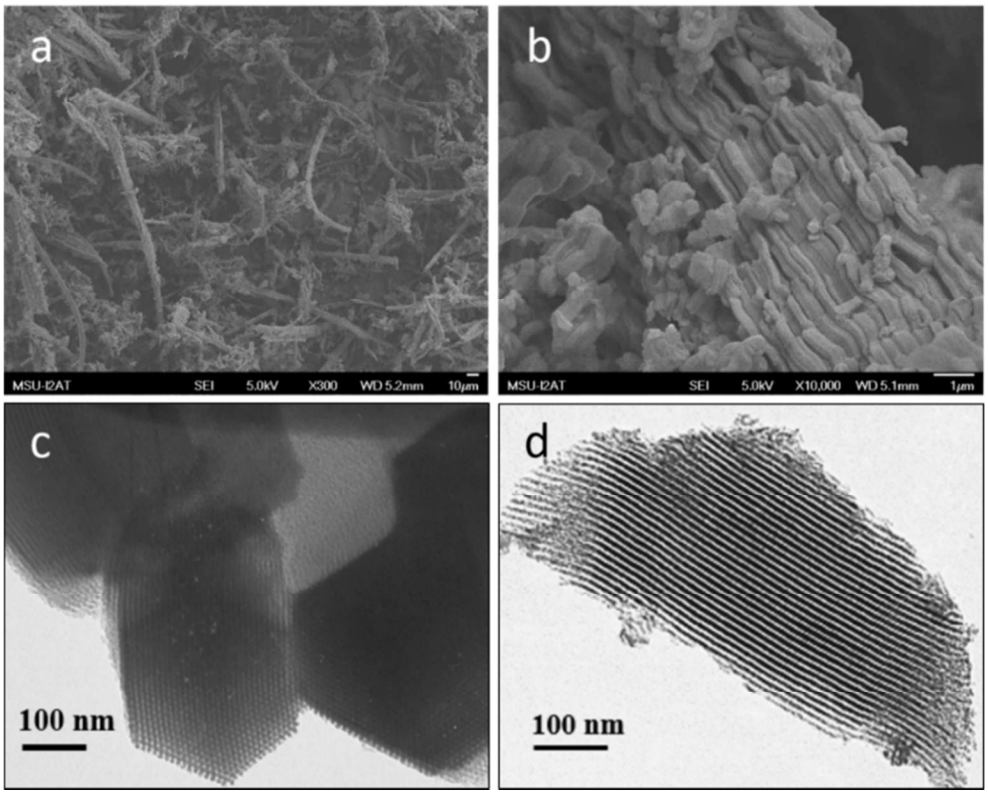

Fig. 2 SEM images of as-synthesized hexagonal mesoporous silica SBA-15 at (a) low magnification and (b) high magnification, and TEM images of SBA-15 by the direction of (c) parallel and (d) perpendicular.

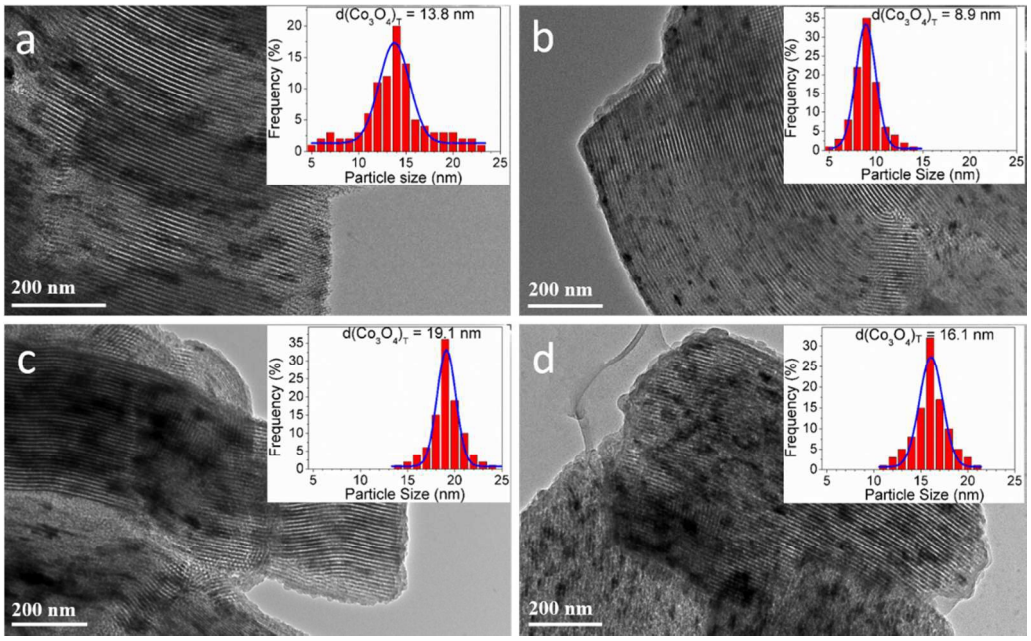

Fig. 3 HRTEM images of calcined 20Co/SBA-15 catalysts (a) 20Co/SBA-15(P1), (b) 20Co/SBA-15(P2), (c) 20Co/SBA-15(P3), and (d) 20Co/SBA-15(P1). The insets are the cobalt particle size distributions.

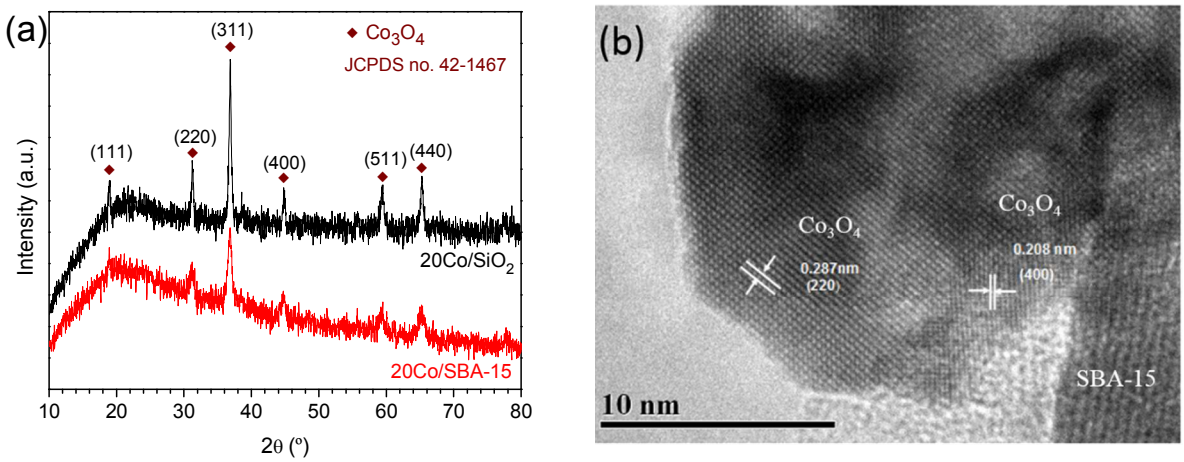

Fig. 4 (a) XRD patterns of calcined 20Co/SiO_2 and 20Co/SBA-15 catalysts, and (b) HRTEM images of 20Co/SBA-15 catalyst.

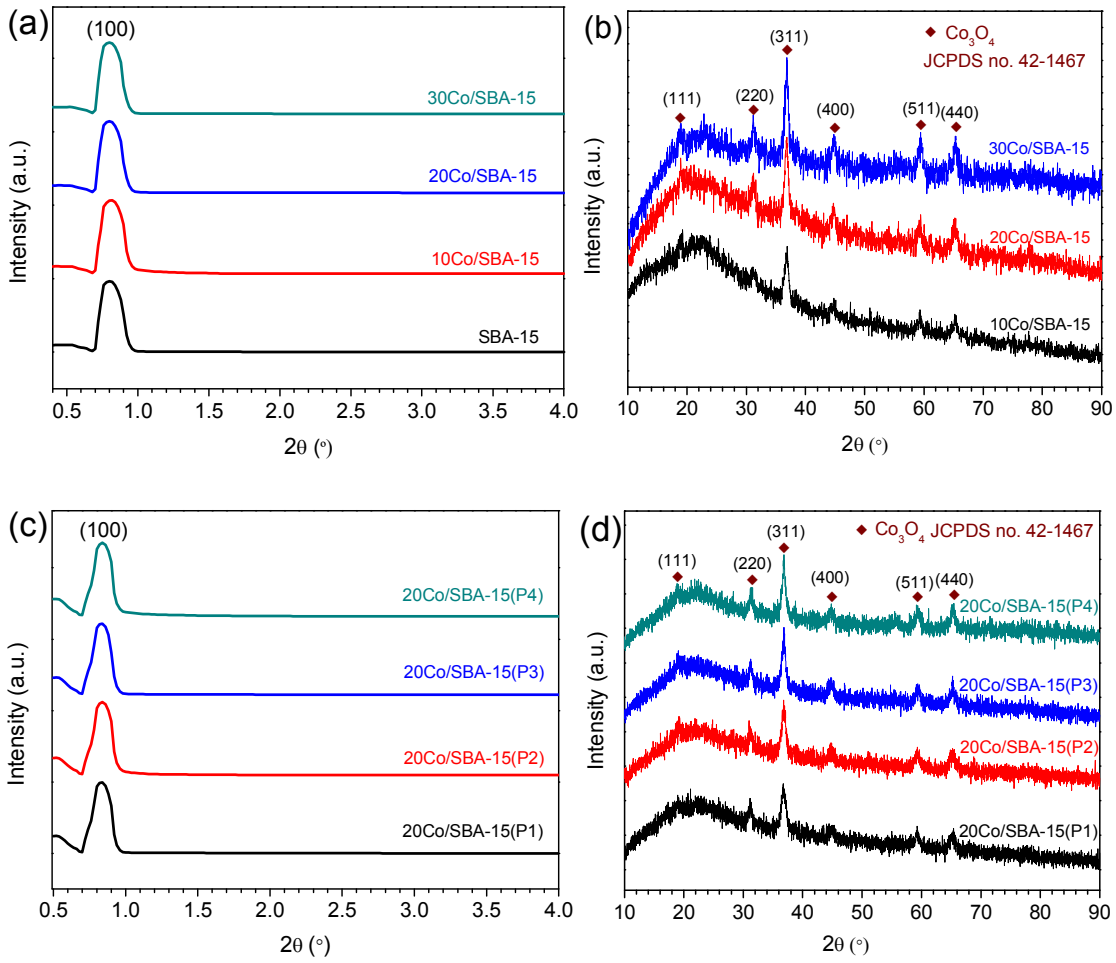

Fig. 5 (a) Small-angle XRD patterns of SBA-15 and Co/SBA-15 catalysts with different cobalt loadings, (b) high-angle XRD patterns of Co/SBA-15 with different cobalt loadings, (c) small-angle and (d) high-angle XRD patterns of Co/SBA-15 catalysts with different pore sizes of SBA-15 support.

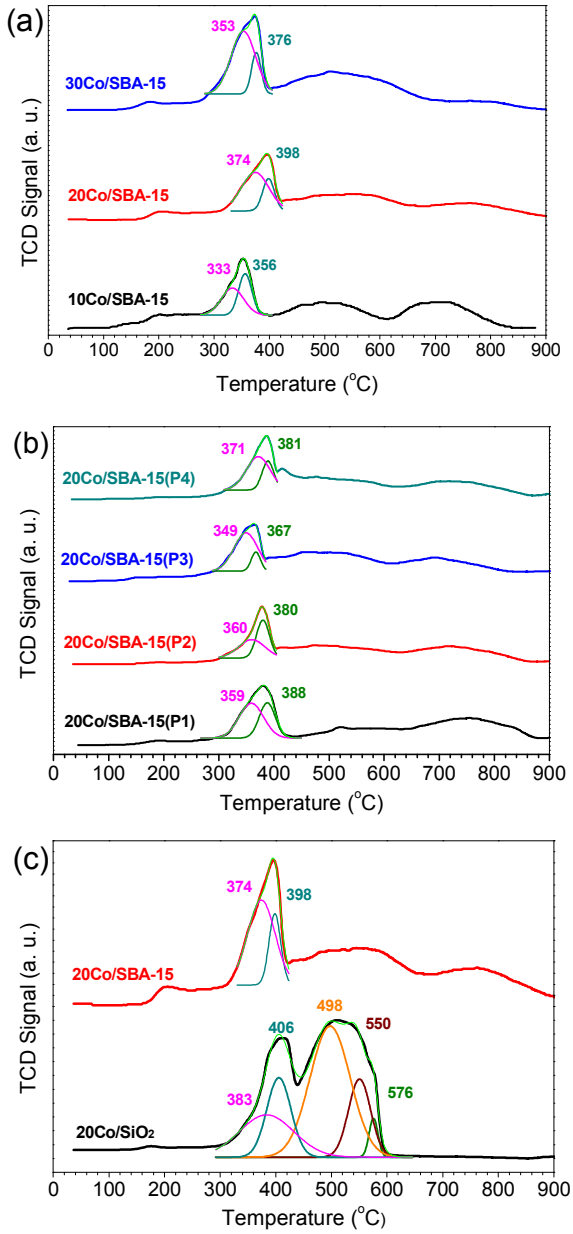

Fig. 6. Temperature programmed reduction profiles of calcined cobalt catalysts.

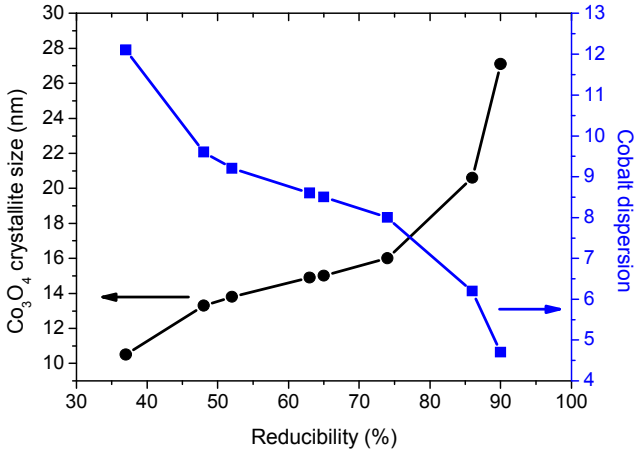

Fig. 7 Relationship between Co_3O_4 crystallite size, cobalt dispersion and its reducibility.

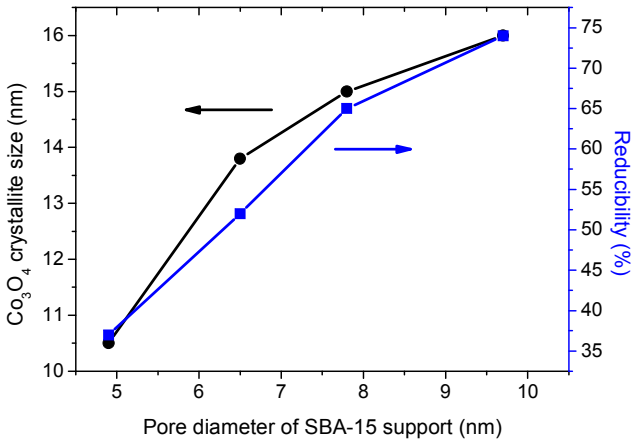

Fig. 8 Dependences of Co_3O_4 crystallite sizes and extents of Co reduction at 400 ℃ on different pore diameters of SBA-15.

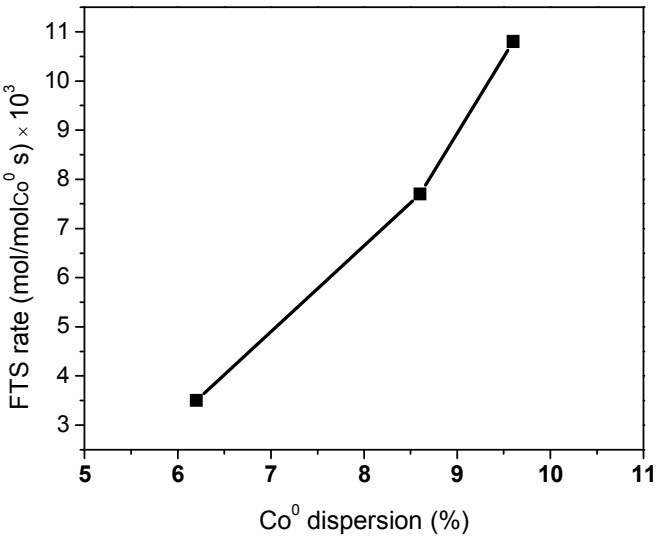

Fig.9 FTS reaction rate based on reduced cobalt with different cobalt loading as a function of Co^0 dispersion.

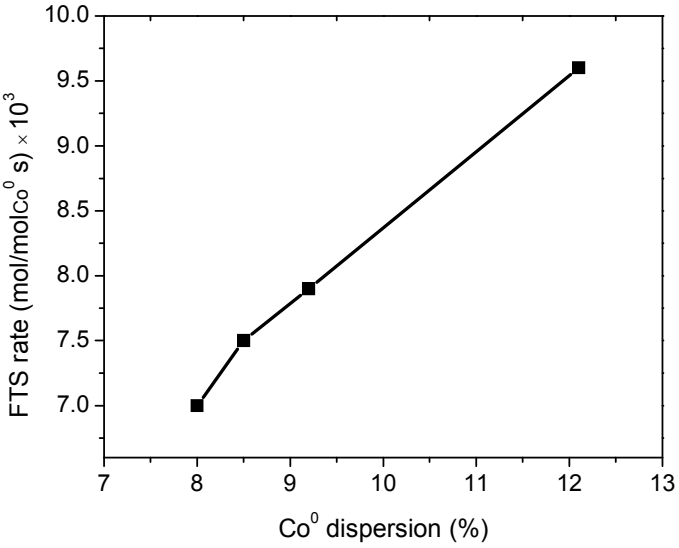

Fig.10 FTS reaction rate based on reduced cobalt with different pore size of SBA-15 support as a function of Co^0 dispersion.

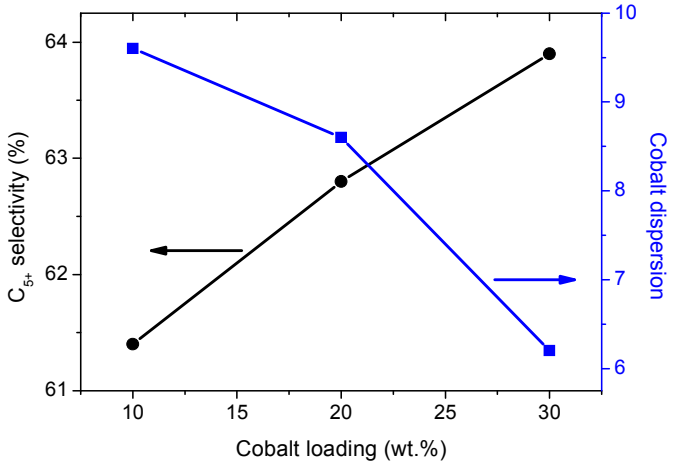

Fig. 11 Effect of cobalt loading on cobalt dispersion and C_{5+} selectivity.

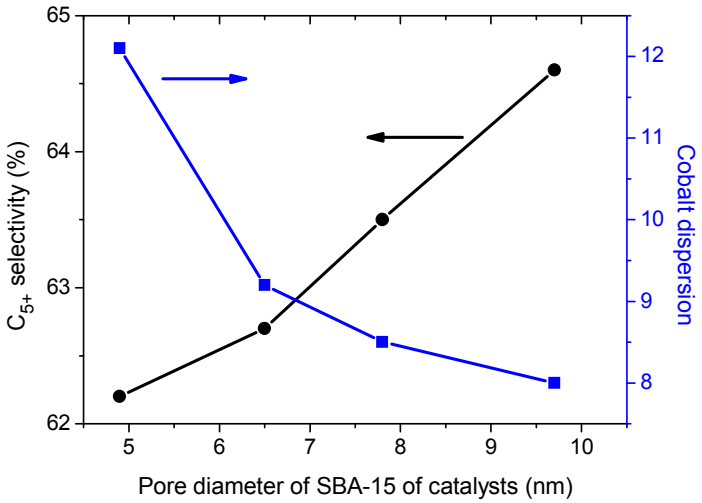

Fig. 12 Effect of pore diameter of SBA-15 on cobalt dispersion and C_{5+} selectivity.

Table 1 Properties of the supports and catalysts determined by N_2 adsorption, XRD and TPR characterization.

Sample	BET surface area (m^2g^{-1})	Pore size (nm)	Pore volume (cm^3g^{-1})	d (Co_3O_4) [a] (nm)	d (Co^0) [b] (nm)	D (Co^0) [c] (%)	Reducibility [d] (%)
SiO_2	154	23.3	1.00	-	-	-	-
20Co/SiO_2	114	15.4	0.88	27.1	20.3	4.7	90
SBA-15	460	8.0	1.85	-	-	-	-
10Co/SBA-15	407	7.8	1.62	13.3	10.0	9.6	48
20Co/SBA-15	384	7.2	1.72	14.9	11.2	8.6	63
30Co/SBA-15	359	7.1	1.36	20.6	15.5	6.2	86
20Co/SBA-15(P1)	457	4.9	0.72	10.5	7.9	12.1	37
20Co/SBA-15(P2)	455	6.5	0.80	13.8	10.4	9.2	52
20Co/SBA-15(P3)	396	7.8	0.85	15.0	11.3	8.5	65
20Co/SBA-15(P4)	354	9.7	0.90	16.0	12.0	8.0	74

[a] Average crystalline size of Co_3O_4 calculated from the Scherrer equation: $d_{(Co_3O_4)} = \frac{0.9\lambda}{B\cos\theta_B} \times \frac{180^\circ}{\pi}$, [b] Average cobalt crystallite size estimated from the corresponding $d_{(Co_3O_4)}$ by applying the molar volume correction: $d_{(Co^0)} = 0.75 \times d_{(Co_3O_4)}$, [c] Dispersion of Co^0: $D_{(Co^0)} = 96/d_{(Co^0)}$,[d] Estimated from H_2 consumption of TPR profiles below 400 ℃.

Table 2 FTS results for Co/SBA-15 catalysts.

Catalyst	CO conversion (%)	Selectivity (wt%)			Hydrocarbon distribution (wt%)			α [c]
		CO_2	ROH [a]	RH [b]	C_1	C_{2-4}	C_{5+}	
20Co/SiO_2	18.8	2.3	10.0	87.7	18.4	19.6	62.0	0.80
10Co/SBA-15	18.3	1.8	7.8	90.4	20.9	17.7	61.4	0.82
20Co/SBA-15	35.6	1.6	6.3	92.1	20.3	16.9	62.8	0.83
30Co/SBA-15	22.4	1.1	5.6	93.3	20.1	16.0	63.9	0.82
20Co/SBA-15(P1)	27.6	1.0	8.2	90.8	21.1	16.7	62.2	0.81
20Co/SBA-15(P2)	34.5	1.7	6.3	92.0	20.5	16.8	62.7	0.81
20Co/SBA-15(P3)	40.3	0.6	6.0	93.4	19.5	17.0	63.5	0.82
20Co/SBA-15(P4)	43.8	0.4	7.0	92.6	19.2	16.2	64.6	0.83

Reaction conditions: P = 290 psig, T = 245 ℃, H_2/CO = 2, GHSV = 2000 h^{-1}. [a] ROH for alcohol, [b] RH for hydrocarbon, and [c] chain growth probability obtained from the ASF plot in the C_8–C_{14} hydrocarbons range.